MATERIALS CHEMISTRY FRONTIERS

RESEARCH ARTICLE

View Article Online
View Journal | View Issue



Cite this: *Mater. Chem. Front.*, 2024, **8**, 2173

# Simultaneously excited downshifting/upconversion luminescence from lanthanide-doped core–shell lead-free perovskite nanocrystals for encryption and data storage†

Endian Cui,‡[b] Gaoyuan Xing,‡[b] Xiangyang Yuan,[b] Yi Zhang,[b] Flavia Artizzu,[e] Xiaoling Liao,[b] Jianfeng Tang,[b] Yanan Zhao,[c] Pengzhou Zhao,[a] Kai Liu*[d] and Jing Liu*[a]

Received 5th October 2023,
Accepted 2nd February 2024

DOI: 10.1039/d3qm01077e

rsc.li/frontiers-materials



Metal ion doping is the most viable method to modulate the optical properties of lead-free $Cs_2AgInCl_6$ double perovskite (DP) nanocrystals (NCs). However, despite the fact that doping multiple cations can allow for emission color tuning, their random distribution into the perovskite matrix poses severe limitations caused by uncontrollable and adverse energy interactions between the dopants, resulting in poor emission color purity and photoluminescence (PL) quenching. To address this issue, we designed $Cs_2AgInCl_6$-based core–shell NCs doped with different metal ions in the two layers *via* an epitaxial growth strategy, with the aim to spatially separate the diverse optically active centers. We selected $Cs_2AgInCl_6$:Bi as the core and $Cs_2AgInCl_6$:Yb, Er as the shell and successfully constructed $Cs_2AgInCl_6$:Bi@$Cs_2AgInCl_6$:Yb, Er core–shell NCs. The so-designed core–shell NCs allow for non-interacting dual-modal luminescence (upconversion/downshifting) yielding not only broadband self-trapping exciton orange emission under ultraviolet (370 nm) excitation but also upconversion green light emission under near-infrared (980 nm) excitation, so far unprecedented in DP NCs. Taking advantage of the high photostability and stability against moisture bestowed by the shell coating, we demonstrate that the resulting core–shell DP NCs can be successfully employed as luminescent ink for dual-mode anti-counterfeiting labels. These results not only provide a novel design strategy for multi-emissive lead-free NCs, but can also represent a milestone to realize controllable luminescent materials for anti-counterfeiting and information storage.

## Introduction

Double perovskite (DP) $Cs_2AgInCl_6$ nanocrystals (NCs) are attracting much interest as a replacement for the classic and toxic lead halide $CsPbX_3$ perovskites for optical and optoelectronic applications, because of their superior environmental stability, widely tunable direct bandgap and achievable broadband self-trapping exciton (STE) emission. However, their low photoluminescence (PL) intensity, single emission band and lack of near-infrared (NIR) photoexcitation limit their further development.[1–6] It has been shown that the incorporation of metal ions, including d- and p-metal and 4f-lanthanide ions ($Ln^{3+}$), is an effective strategy to expand the luminescent properties of DPs in the visible and near-infrared (NIR) spectral regions.[7–12] However, current research mainly focuses on the traditional single fluorescence mode, only featuring downshifted (UV-Vis to Vis/NIR) monotonous emission with non-tunable optical characteristics, whereas the realization of upconversion (NIR to Vis) emission still remains a challenge.[13] These inherent limitations greatly hinder the applications of DP materials in information security. Therefore, it is highly desirable to endow $Cs_2AgInCl_6$ NCs with various and controllable optical modes by bringing together both downshifting and upconversion luminescence mechanisms simultaneously,[14–16] to realize photonic devices for data encryption and storage.

[a] *Department of Oncology, The People's Hospital of JiangMen, Jiangmen, 529000, China. E-mail: jingliu77@swu.edu.cn*
[b] *Key Laboratory of Luminescence Analysis and Molecular Sensing, Ministry of Education, School of Materials and Energy, Southwest University, Chongqing, 400715, China*
[c] *Analytical and Testing Center, Southwest University, Chongqing, 400715, China*
[d] *College of Materials Science and Engineering, Chongqing Jiaotong University, Chongqing, 400074, China. E-mail: kai.liu@cqjtu.edu.cn*
[e] *Department of Sustainable Development and Ecological Transition (DISSTE), University of Eastern Piedmont "A. Avogadro", Piazza S. Eusebio 5, Vercelli, 13100, Italy*

† Electronic supplementary information (ESI) available. See DOI: https://doi.org/10.1039/d3qm01077e

‡ Endian Cui and Gaoyuan Xing contributed equally.

Among the metal ion dopants yielding downshifted broadband luminescence, $Bi^{3+}$ is particularly popular because of its excellent stability and environmental friendliness.[17–19] The incorporation of $Bi^{3+}$ with its outermost $ns^2$ electrons into $Cs_2AgInCl_6$ DP allows for tailoring the projected boundary state, leading to significant changes in the optical absorption and emission properties and realizing STE downshifted visible luminescence under UV excitation.[20,21] On the other hand, 4f-metal ions, whose emission, originating from intra-shell f–f transitions, is characterized by high color purity and long-lifetimes, can in principle allow for narrow-band upconversion luminescence in the visible upon NIR excitation.[22] Among the $Ln^{3+}$ ions, $Yb^{3+}$, which can be photoexcited at 980 nm, is often coupled as a sensitizer with the $Er^{3+}$ activator to yield high color purity green upconversion emission.[23–25] Chen's group incorporated $Yb^{3+}$ and $Er^{3+}$ into $Cs_2AgBiCl_6$ DP attempting to achieve upconversion and downshifting dual-mode PL; however, the coupling of the energy levels of $Bi^{3+}$ and $Er^{3+}$ led to a yellow-green light emission with poor color purity.[26,27] Therefore, although $Ln^{3+}$ and transition metal ion doping can endow $Cs_2AgInCl_6$ NCs with excellent optical performance, the limited color purity caused by the energy level coupling and uncontrollable energy transfer pathways between the dopants still remains to be solved, but this aspect is still lacking researchers' attention.

To overcome the issue mentioned above, it is necessary to spatially separate the downshifting and upconversion emission centers. Efforts from this field mainly focused on the mechanical mixing of upconversion fluoride nanoparticles and perovskite NCs. Zhang's group designed a nanocomposite composed of $CsPbX_3$ perovskite NCs decorated with upconversion $Yb^{3+}/Er^{3+}$ doped $NaYF_4$ fluoride nanoparticles to achieve downshifting/upconversion dual-mode emission, but the nanocomposite needs to be mixed with prepolystyrene to improve its stability to light and water, due to the absence of protection derived from the heterogeneous structure.[28] The most striking limitation of this approach comes from the fact that the establishment of heterogeneous core–shell structures to assemble fluoride and perovskite hosts is nearly inaccessible due to the lattice mismatch of the components.[29–31]

In this work, we successfully designed DP only core–shell nanostructures based on $Cs_2AgInCl_6$, with the aim to confine the upconversion and downshifting emissive centers achieving excellent multimodal optical properties and good environmental tolerance while avoiding the structural instability induced by lattice mismatch. We selected $Cs_2AgInCl_6$ : 2%Bi NCs as core, and $Cs_2AgInCl_6$ : 20%Yb, 7%Er NCs as shell to construct $Cs_2AgInCl_6$ : 2%Bi@$Cs_2AgInCl_6$ : 20%Yb, 7%Er core–shell DP NCs by an epitaxial growth method. Under 370 nm excitation, the core–shell NCs display bright orange light stemming from the STEs emission of the $Bi^{3+}$ doped core, while 980 nm photoexcitation triggers green light upconverted emission with high color purity. The successful establishment of core–shell structured DP NCs not only realizes multi-mode PL in the visible region with high color purity under UV/NIR excitation, but also further improves the stability of the DP NCs. Thanks to the combination of these properties, the designed core–shell DP NCs are suitable for the practical application in the field of dual-modal luminescence anti-counterfeiting, which we demonstrate through the successful realization of a prototype information storage and encryption system working under UV and NIR light illumination.

# Experimental

### Materials and chemicals

Silver acetate (Ag(ac), 99.95%), indium(III) acetate ($In(ac)_3$, 99.99%), bismuth(III) acetate ($Bi(ac)_3$, 99.99%), ytterbium(III) acetate ($Yb(ac)_3$, 99.9%), erbium(III) acetate ($Er(ac)_3$, 99.99%), cesium carbonate ($Cs_2CO_3$, 99.99%), oleic acid (OA, 90%), oleylamine (Olam, 90%), cyclohexane (99%), benzoyl chloride (Bz-Cl, 99%), and diphenyl ether (DPE, 99.9%) were all purchased from Aladdin. All chemicals were directly used without any further purification.

### Synthesis of Cs-oleate

$Cs_2CO_3$ (1630 mg) and OA (20 mL) were loaded into a 50 mL three-necked flask, then heated to 100 °C at a rate of 10 °C $min^{-1}$ and degassed under vacuum for 40 min. The mixture was then heated to 150 °C in an $N_2$ atmosphere and reacted for 3 h until the solution became clear. Finally, the obtained solution was cooled to room temperature and stored in a light-protected glass vial.

### Synthesis of undoped and $Bi^{3+}$ doped $Cs_2AgInCl_6$ NCs (denoted as *x*%Bi)

In a typical synthesis, $In(ac)_3$ (0.25 mmol), Ag(ac) (0.2 mmol), Olam (0.5 mL), Cs-oleate solution (1 mL), and DPE (4 mL) were added into a 50 ml three-necked flask and degassed under vacuum for 30 min. The mixed solution was heated up to 120 °C at a ramping rate of 10 °C $min^{-1}$ under $N_2$ atmosphere, then 0.5 mL of degassed DPE thoroughly mixed with 0.25 mL of Bz-Cl was swiftly injected into the three-necked flask. The flask was immersed in an ice-water bath for 15 s to quench the reaction. The obtained crude solution was centrifuged at 10 000 rpm for 5 min. The supernatant was discarded, and the residues were redispersed in 3 mL of cyclohexane and washed with ethyl acetate. The washing step was repeated at least twice. *x*%Bi NCs (the molar concentration of the prepared samples is 0.02 mol $L^{-1}$) were synthesized through a similar procedure as mentioned above, except adding the appropriate quantities of $Bi(ac)_3$ to the initial reaction mixture (*x* = Bi/In precursors percentage of 0.5, 1, 2, 5, and 10).

### Synthesis of $Yb^{3+}$, $Er^{3+}$ co-doped $Cs_2AgInCl_6$ NCs (denoted as 20%Yb, *x*%Er)

20%Yb, *x*%Er NCs (the molar concentration of the prepared samples is 0.02 mol $L^{-1}$) were synthesized following a similar protocol, except employing 0.05 mmol of $Yb(ac)_3$ and adding the appropriate amounts of $Er(ac)_3$ to the initial reaction mixture (*x* = Er/In precursors percentage of 1, 3, 5, 7, and 10).

 

### Synthesis of $Bi^{3+}$, $Yb^{3+}$, $Er^{3+}$ co-doped $Cs_2AgInCl_6$ NCs (denoted as 2%Bi, 20%Yb, 7%Er)

2%Bi, 20%Yb, 7%Er NCs (the molar concentration of the prepared samples is 0.02 mol $L^{-1}$) were synthesized following a similar protocol, except employing 0.1775 mmol of $In(ac)_3$ in the initial reaction mixture.

### Synthesis of $Cs_2AgInCl_6$ : 2%Bi core NCs (denoted as 2%Bi)

2%Bi NCs were synthesized by adopting the same protocol as mentioned in the synthesis of $Bi^{3+}$ doped $Cs_2AgInCl_6$ NCs, and the as-prepared NCs were dispersed in 1 mL of cyclohexane for storage.

### Synthesis of $Cs_2AgInCl_6$ : 2%Bi@$Cs_2AgInCl_6$ : 20%Yb, 7%Er core–shell NCs (denoted as 2%Bi@20%Yb, 7%Er)

Typically, $In(ac)_3$ (0.1825 mmol), Ag(ac) (0.2 mmol), $Yb(ac)_3$ (0.05 mmol), $Er(ac)_3$ (0.0175 mmol), Olam (0.5 mL), Cs-oleate solution (1 mL), and DPE (4 mL) were loaded into a 50 mL three-necked flask, and degassed under vacuum for 30 min. Then, the temperature was increased to 60 °C at a heating rate of 5 °C $min^{-1}$ under a $N_2$ atmosphere. Meanwhile, 2%Bi NCs (1 mL) were rapidly injected into the flask and degassed under vacuum for 30 min to remove the cyclohexane. The temperature was then increased to 120 °C at a heating rate of 10 °C $min^{-1}$ under a $N_2$ atmosphere, following which 0.5 mL of degassed DPE thoroughly mixed with 0.25 mL of Bz-Cl was swiftly injected into the three-necked flask. The flask was immersed in an ice-water bath for 15 s to quench the reaction. The resulting crude solution was centrifuged at 10 000 rpm for 5 min, and the supernatant was discarded. The residues were redispersed in 3 mL of cyclohexane and washed with ethyl acetate. The washing step was repeated at least twice (the molar concentration of the prepared samples is 0.02 mol $L^{-1}$).

### Characterization

The X-ray diffraction (XRD, XRD-7000) patterns were collected using a Shimadzu X-ray diffractometer with Cu Kα radiation ($\lambda$ = 1.54 Å). Transmission electron microscopy (TEM) images, high-resolution TEM (HRTEM) images, energy-dispersive X-ray spectroscopy (EDS) spectra and selected area electron diffraction patterns (SAED) of the samples were obtained using a JEM-F200 electron microscope. The UV-Vis absorption spectra were measured using a Hitachi UH4150 in the range of 200–800 nm. The PL spectra and decay curves of samples were collected using an Edinburgh fluorescence spectrometer FLS1000. Inductively coupled plasma-optical emission spectrometry (ICP-OES) data were recorded using an Agilent 5110 optical emission spectrometer. The X-ray photoelectron spectroscopy (XPS) data were taken by a Thermo Scientific K-Alpha using a monochromatic Al Kα source. The thermogravimetric (TG) measurements were performed using a PerkinElmer STA-8000 in the temperature range from 30 °C to 800 °C, at a ramping rate of 10 °C $min^{-1}$ under Ar flow (20 mL $min^{-1}$).

## Results and discussion

The pristine $Cs_2AgInCl_6$ and its doped counterparts (2%Bi, 20%Yb, 7%Er), as well as the core–shell structured 2%Bi@20%Yb, 7%Er, have been successfully synthesized *via* a modified thermal injection method.[19] Their crystal structures have been characterized by XRD. As seen in Fig. 1a, all the samples exhibit high crystallinity, and the XRD diffraction peaks can be classified as a cubic DP (ICSD No. 257115). The consilience of XRD patterns indicates that there is no detectable impurity introduced into the DP with the employed $Ln^{3+}$ doping method. The diffraction peak of the (220) plane of $Ln^{3+}$-doped samples around $2\theta$ = 24° is slightly shifted towards the smaller-angle region compared to that of the pristine $Cs_2AgInCl_6$ (Fig. 1a), which may be attributed to the replacement of $In^{3+}$ with $Bi^{3+}$, $Yb^{3+}$ and $Er^{3+}$.[10,32] The lattice parameters and unit cell volume of the DP NCs, summarized in Table S1 (ESI†), gradually increase as the dopants are introduced. Fig. 1b represents a schematic crystal structure of $Bi^{3+}$-doped and $Yb^{3+}$, $Er^{3+}$ co-doped $Cs_2AgInCl_6$ unit cells, which are constituted by $Cs^+$ ions, $[AgCl_6]^{5-}$, $[InCl_6]^{3-}$, $[BiCl_6]^{3-}$, $[YbCl_6]^{3-}$ and $[ErCl_6]^{3-}$ octahedra, depending on the crystal composition. As illustrated, some of the $In^{3+}$ sites are occupied by the dopants.[18,25,26,33]

XPS data in Fig. S1a–c (ESI†) show that all the samples contain Cl, Cs, Ag, and In elements, whereas high-resolution spectra prove the presence of Bi, Yb, Er in the core–shell NCs, as seen in Fig. S1d–f (ESI†). In addition, Fig. S1b and c (ESI†) indicate that the characteristic peaks of In $3d_{3/2}$ and In $3d_{5/2}$ in $Ln^{3+}$-doped NCs are slightly shifted towards the higher binding energy region compared to the pristine sample, while there is no obvious change in the Ag 3d peak. This may be ascribed to the lattice expansion resulting from the successful incorporation of $Ln^{3+}$, as $Yb^{3+}$ and $Er^{3+}$ occupy the $In^{3+}$ sites rather than the $Ag^+$ sites.[10] The presence of Bi, Yb, and Er elements in the as-prepared NCs is also confirmed by ICP-OES measurements, and the atomic ratios of Cs/In, Bi/In, Yb/In, and Er/In in different samples are shown in Table S2 (ESI†).

The detailed morphologies of the as-prepared NCs have been investigated by TEM. The synthesized NCs with different doping contents all exhibit similarly uniform cubic morphologies and high crystallinity (Fig. 2). The average sizes of the NCs are altered on variations of the composition but maintain a homogeneous distribution (Fig. S2, ESI†). In addition, HRTEM

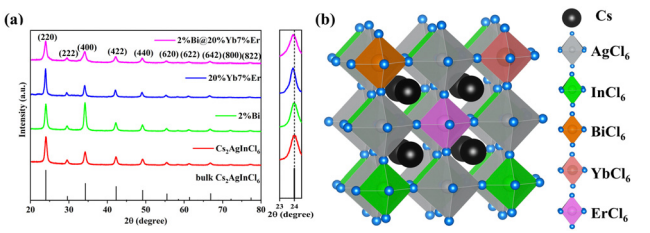


Fig. 1 (a) XRD patterns of $Cs_2AgInCl_6$, $Cs_2AgInCl_6$:2%Bi (denoted as 2%Bi), $Cs_2AgInCl_6$:20%Yb, 7%Er (denoted as 20%Yb, 7%Er) and $Cs_2AgInCl_6$:2%Bi@$Cs_2AgInCl_6$:20%Yb, 7%Er (denoted as 2%Bi@20%Yb, 7%Er) NCs (left) and the zoomed-in XRD patterns in the range of 23–24.5° (right); (b) schematic structure illustrating the unit cells of $Bi^{3+}$-doped $Cs_2AgInCl_6$ and $Yb^{3+}$, $Er^{3+}$ co-doped $Cs_2AgInCl_6$ for brevity.

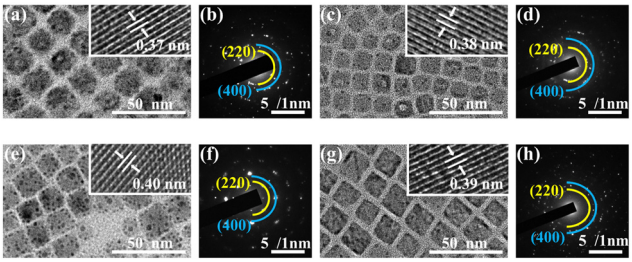


Fig. 2 TEM and HRTEM images (insets) of (a) $Cs_2AgInCl_6$, (c) 2%Bi, (e) 20%Yb, 7%Er and (g) 2%Bi@20%Yb, 7%Er NCs, and their corresponding SAED patterns (b), (d), (f) and (h). Some 'dark dots' appearing in the TEM images over the surface of the NCs are attributable to the reduction of $Ag^+$ to $Ag^0$ by Olam.[21,34]

images in the insets of Fig. 2(a, c, e and g) show that the lattice spacing of the (220) crystal plane is increased from 0.37 nm to 0.38 nm, 0.40 nm and 0.39 nm depending on the doped cations, which is consistent with the lattice expansion validated by the XRD analysis. The SAED patterns, shown in Fig. 2(b, d, f and h), illustrate the presence of (220) and (400) planes of the cubic structure, revealing the consistent DP structure of as-prepared nanocrystals. The TEM-EDS results in Fig. S3 (ESI†) indicate that the nanocubes are well-constructed with evenly distributed elements, whose content is consistent with the ICP data. The particle size of the core-only 2%Bi NCs is 11.9 nm, while the size of 2%Bi@20%Yb, 7%Er NCs is 15.2 nm. The EDS mapping of 2%Bi@20%Yb, 7%Er NCs is shown in Fig. S3 (ESI†). We investigated the XRD pattern and TEM images of a physical mixture of 2%Bi and 20%Yb, 7%Er NCs (Fig. S4, ESI†) to reveal the microstructural difference in contrast. As seen in the XRD pattern, the physical mixture exhibits the cubic DP structure (ICSD No. 257115) without detectable impurities. Compared to the well-defined core–shell structured DP NCs (Fig. 2g), the NCs with different dopants are randomly distributed in the physical mixture, leading to strong irregularity in morphologies and sizes (Fig. S4b, ESI†). Thus, based on the combination of the TEM, XRD and XPS investigation, it is possible to conclude that the seeded growth method adopted in this work was successful for the synthesis of the designed core–shell DP NCs.

As shown in Fig. 3, the optical features of both the $Bi^{3+}$-doped and the $Yb^{3+}$, $Er^{3+}$ co-doped DP NCs are fully preserved in the constructed core–shell NCs (Fig. S7 and S8, ESI†). The core–shell DP NCs present excitation-dependent multicolor emission properties, yielding a broadband STE orange emission peaked at around 690 nm under 370 nm excitation (Fig. 3a) and narrow emission peaks at 524 nm, 550 nm and 659 nm, corresponding to green light (Fig. 3b) when illuminated with 980 nm light. The possible PL mechanisms are shown in Fig. 3c and d (detailed in the ESI†). The CIE coordinates of the core–shell $Cs_2AgInCl_6$ NCs at different excitation wavelengths (Fig. S10a, ESI†) show that the core–shell NCs display strikingly different orange and green colors when excited with UV and NIR light, respectively.

In fact, the spatial separation and confinement of the down-shifting and upconversion emitting centers in such layered

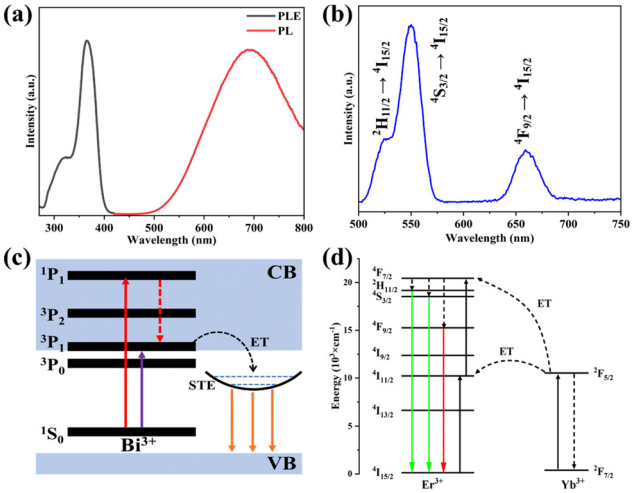


Fig. 3 PL properties of 2%Bi@20%Yb, 7%Er. (a) PL ($\lambda_{ex}$ = 370 nm) and PLE ($\lambda_{em}$ = 690 nm) spectra; (b) PL ($\lambda_{ex}$ = 980 nm) spectrum; (c) schematic diagram of the energy-transfer mechanism of $Bi^{3+}$ in core–shell NCs; (d) schematic diagram of the energy-transfer mechanism of $Yb^{3+}$–$Er^{3+}$ in core–shell NCs.

nanostructures allows for successfully ruling out adverse energy interactions and uncontrollable energy transfer pathways, especially between $Bi^{3+}$ and $Er^{3+}$, leading to poor color purity PL and PL quenching. To confirm this conclusion, we compared the PL properties of 2%Bi@20%Yb, 7%Er, 2%Bi and 2%Bi, 20%Yb, 7%Er NCs. As expected, the emission intensity upon 370 nm excitation of core–shell NCs is significantly stronger than that of 2%Bi and 2%Bi, 20%Yb, 7%Er NCs (Fig. 4a and b), whereas the PL quantum yield (PLQY) of core–shell NCs increases to 7.4% compared to the 2.2% value retrieved for 2%Bi, 20%Yb, 7%Er NCs. This indicates that the spatial separation of the diverse optically active centers in the constructed core–shell structure ultimately improves the PL performance of DP NCs. To further prove this conclusion, we performed time-resolved

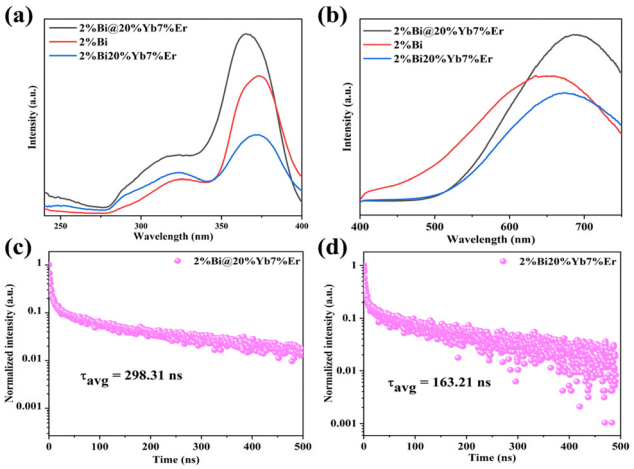


Fig. 4 (a) and (b) The PLE and PL spectra of 2%Bi@20%Yb, 7%Er, 2%Bi and 2%Bi, 20%Yb, 7%Er NCs; (c) and (d) PL decay curves of 2%Bi@20%Yb, 7%Er and 2%Bi, 20%Yb, 7%Er NCs emission at around 690 nm under 375 nm excitation.

 

PL measurements of 2%Bi@20%Yb, 7%Er NCs and 2%Bi, 20%Yb, 7%Er NCs at 690 nm (Fig. 4c and d). It is observed that the retrieved lifetime ($\tau_{avg}$) of 2%Bi, 2%Yb, 7%Er NCs is reduced to 163.21 ns compared with 2%Bi NCs ($\tau_{avg}$ = 195.64 ns) likely due to a competitive and uncontrolled energy transfer between $Bi^{3+}$ and $Er^{3+}$ (Fig. S7d, ESI†), which quenches the emission. On the other hand, the average lifetime ($\tau_{avg}$) of core–shell NCs remarkably increases up to 298.31 ns, leading to the observed increased PLQY and emission intensity.

Additionally, the core–shell structured NCs are beneficial in broadening the absorption and excitation ranges (Fig. 4a and Fig. S5b, ESI†). Meanwhile, we can observe from the PLE spectra (Fig. 4a) the two broad excitation peaks of the three samples are centered at approximately 320 nm and 370 nm. The former was attributed to the sub-band gap shallow trap state, while the latter was attributed to the spin-allowed $^1S_0 \rightarrow {}^3P_1$ transition of $Bi^{3+}$.[20] Interestingly, the PLE spectrum of 2%Bi@20%Yb, 7%Er NCs showed a blue shift compared to the others', which could be attributed to the reduced surface defects by the construction of the core–shell structure.[28,31,35,36]

In addition, the construction of core–shell NCs is an effective strategy to protect the active core (2%Bi), improving the structural and optical stability of DP NCs. Compared with the physical mixture of bare 2%Bi and 20%Yb, 7%Er NCs as well as the naked 2%Bi NCs, the constructed core–shell NCs exhibit an overall improvement in PL stability under various conditions, *e.g.* moisture, continuous UV light irradiation and high temperatures (Fig. 5). The molar concentration of the prepared samples is all 0.02 mol $L^{-1}$. The luminescence intensity was recorded as a function of time in a moisture environment (0.1 mL of DI water was added to 0.9 mL of 2%Bi@20%Yb, 7%Er core–shell NCs, the mixture of 2%Bi NCs and 20%Yb, 7%Er NCs and 2%Bi NCs cyclohexane solutions, respectively) or under UV light irradiation. The luminescence intensity was measured at different temperatures from 20 to 80 °C. As the boiling point of cyclohexane is around 80.7 °C, we set the maximum tested temperature to 80 °C. First, The core–shell structured NCs show superior optical stability in moisture, as their normalized PL intensity remains above 0.2 for 90 minutes, while the naked particles are nearly quenched (Fig. 5a). Similarly, under long-time UV irradiation (Fig. 5b), the core–shell NCs present much slower decay than the other NCs in the entire period of investigation (300 minutes). Finally, upon temperature increase (20–80 °C), the PL intensity of bare 2%Bi NCs rapidly declines below 0.3 at 50 °C, and further decreases to below 0.1 above this point, while the PL intensity of core–shell NCs remains above that of the nanocrystal mixture in the range from 30 °C to 80 °C, with a much slower decrease trend (Fig. 5c). These results indicate that effective protection of $Bi^{3+}$-doped $Cs_2AgInCl_6$ DP NCs from external perturbing agents is realized by the designed core–shell structure.

To demonstrate the feasibility and applicability of core–shell DP NCs in information storage and anti-counterfeiting, we designed a series of patterns taking advantage of the dual-mode PL (upconversion and downshifting) properties, as shown in Fig. 6. 2%Bi(I), 20%Yb, 7%Er(II) and 2%Bi@20%Yb, 7%Er(III) NCs were dispersed in cyclohexane to obtain a fluorescent ink, then deposited on 5 × 5 mm silicon wafers to display the elementary information (Fig. 6a). As shown, there is no color change observed on all three types of materials under daylight irradiation. Under 365 nm excitation, material I and material III emitted orange light, and material II emitted whitish light stemming from the $Cs_2AgInCl_6$ matrix (Fig. S9, ESI†). Under 980 nm excitation, only materials II and III emitted green light. Each silicon wafer coated with PL material acts as a basic module displaying optical signals. The designed pattern is constituted by these pixel-like modules that exhibit preloaded information under a specific excitation mode. As shown in Fig. 6b, the optical signal modules of materials I and III were arranged into a 5 × 11 array in a specific order. When

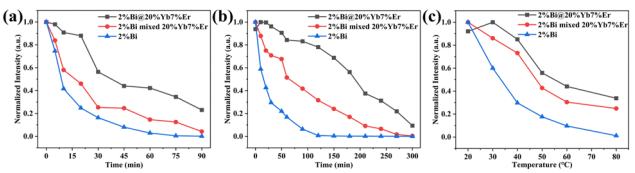


Fig. 5 Comparison of the PL intensity of 2%Bi@20%Yb, 7%Er core–shell NCs, the mixture of 2%Bi NCs and 20%Yb, 7%Er NCs and 2%Bi NCs under 370 nm excitation: (a) in cyclohexane and DI water (v/v = 1 : 9) mixed solvents under 370 nm excitation; (b) under continuous UV light irradiation; (c) at different temperatures.

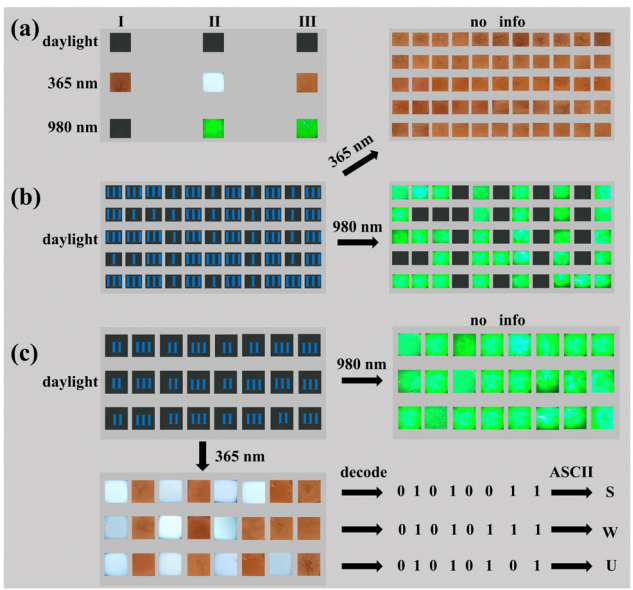


Fig. 6 Storage and decoding of optical information. (a) PL photographs of different NCs deposited on silicon wafers (5 × 5 mm) under the illumination of daylight, 365 nm and 980 nm light, respectively (I: 2%Bi NCs, II: 20%Yb, 7% Er NCs, III: 2%Bi@20%Yb, 7%Er NCs); (b) under the 365 nm and 980 nm excitation, the PL signals of materials I and III display the preloaded information "S", "W", "U"; (c) under 365 nm and 980 nm excitation, the PL signals of materials II and III were converted into ASCII codes and read the preload information "S", "W", "U".

illuminated at 365 nm excitation wavelength, all the modules displayed an orange color. Under 980 nm light irradiation, the modules coated with material I showed no response, while the other modules emitted green light owing to the presence of core–shell DP (material III). As a consequence, the whole array exhibits the preloaded information (''S'', ''W'', ''U'') in contrast, which proves the feasibility of the as-prepared materials for information storage.

Besides the storage/display of directly readable characters, such luminescent materials can also be utilized to store the information encoded with 8-bit ASCII code for future integration with electronic systems, as shown in Fig. 6c. When they were exposed to 365 nm light, the modules containing material II and III emitted white and orange light, respectively. Thus, according to the sequence of emission colors, the information embedded in the three module arrays can be decoded as ''S'', ''W'', ''U''. When excited at 980 nm, all modules only emitted visible green light, protecting the stored information. The above results further prove that the investigated core–shell NCs possess a great application prospect in the fields of anti-counterfeiting and information storage, and the dual-mode emission characteristics of preloaded information can also play a vital role in improving the level of information security.

## Conclusions

In summary, novel luminescent lead-free $Cs_2AgInCl_6$-based core–shell NCs have been resoundingly synthesized *via* an epitaxial growth method, where a $Cs_2AgInCl_6$:Bi core is surrounded by a $Cs_2AgInCl_6$:Er, Yb shell. The resulting core–shell perovskite NCs exhibit a broadband downshifted STE orange emission under UV excitation related to the incorporation of $Bi^{3+}$ centers; as well as the first time reported green upconversion emission under 980 nm excitation from the $Yb^{3+}$, $Er^{3+}$ combination in the shell. Thanks to the spatial separation and confinement of the luminescent downshifting and upconversion dopant centers, adverse intermetallic interactions and uncontrollable energy transfer pathways are ruled out, resulting in high emission color purity in the visible region under dual-mode excitation. The constructed $Cs_2AgInCl_6$:Bi@$Cs_2AgInCl_6$:Yb, Er core–shell NCs not only allow for controllable wavelength-responsive multi-color emission but also further improve the stability against moisture, light and high temperature exposure of $Cs_2AgInCl_6$ DP NCs. The satisfactory optical and structural features of the obtained luminophores enable promising applications in the fields of anti-counterfeiting and information storage.

## Author contributions

Experiments and original draft – writing were completed by Endian Cui under the guidance of Jing Liu, Kai Liu and Flavia Artizzu. Gaoyuan Xing, Xiangyang Yuan, Yi Zhang, Xiaoling Liao, Jianfeng Tang, Yanan Zhao, and Pengzhou Zhao contributed to the data curation and experimental discussion. Funding acquisition was done by Jing Liu.

## Conflicts of interest

There are no conflicts to declare.

## Acknowledgements

This research was supported by the China Postdoctoral Science Foundation (Grant No. 2022M711514, No. 2022T150298) and the starting grant for talents of Chongqing Jiaotong University. We acknowledge the critical and quantity of testing work supported by the Shiyanjia Lab (**https://www.shiyanjia.com**). We thank the Analytical and Testing Center of Southwest University for their assistance with UV-Vis absorption spectra analysis.

## Notes and references

1 G. Volonakis, A. A. Haghighirad, R. L. Milot, W. H. Sio, M. R. Filip, B. Wenger, M. B. Johnston, L. M. Herz, H. J. Snaith and F. Giustino, Cs2AgInCl6: A new lead-free halide double perovskite with direct band gap, *J. Phys. Chem. Lett.*, 2017, **8**, 772–778.

2 J. Zhou, Z. Xia, M. S. Molokeev, X. Zhang, D. Peng and Q. Liu, Composition design, optical gap and stability investigations of lead-free halide double perovskite $Cs_2AgInCl_6$, *J. Mater. Chem. A*, 2017, **5**, 15031–15037.

3 J. Luo, S. Li, H. Wu, Y. Zhou, Y. Li, J. Liu, J. Li, K. Li, F. Yi, G. Niu and J. Tang, $Cs_2AgInCl_6$ double perovskite single crystals: parity forbidden transitions and their application for sensitive and fast UV photodetectors, *ACS Photonics*, 2018, **5**, 398–405.

4 S. Li, J. Luo, J. Liu and J. Tang, Self-trapped excitons in all-inorganic halide perovskites: Fundamentals, status, and potential applications, *J. Phys. Chem. Lett.*, 2019, **10**, 1999–2007.

5 J. C. Dahl, W. T. Osowiecki, Y. Cai, J. K. Swabeck, Y. Bekenstein, M. Asta, E. M. Chan and A. P. Alivisatos, Probing the stability and band gaps of $Cs_2AgInCl_6$ and $Cs_2AgSbCl_6$ lead-free double perovskite nanocrystals, *Chem. Mater.*, 2019, **31**, 3134–3143.

6 J. Luo, M. Hu, G. Niu and J. Tang, Lead-free halide perovskites and perovskite variants as phosphors toward light-emitting applications, *ACS Appl. Mater. Interfaces*, 2019, **11**, 31575–31584.

7 R. Song, S. Xu, Y. Li, Q. Zhang, Y. Gao, H. Yu, Y. Cao, X. Li, S. Zhang and B. Chen, $Bi^{3+}$ and $Tb^{3+}$ co-doped $Cs_2AgInCl_6$ lead-free double perovskite nanocrystals for detection of temperature and copper ions, *Spectrochim. Acta, Part A*, 2023, **288**, 122181.

8 L. Chen, H. Jiang, Z. Luo, G. Liu, X. Wu, Y. Liu, P. Sun and J. Jiang, Enhancement of the efficiency and thermal stability

 

of the double perovskite $Cs_2AgInCl_6$ single crystal by Sc substitution, *Mater. Adv.*, 2022, **3**, 4381–4386.

9 S. Wang, R. Shi, B. Tang, Y. Xiong, A. Portniagin, X. Zhao, S. V. Kershaw, R. Long and A. L. Rogach, Co-doping of tellurium with bismuth enhances stability and photoluminescence quantum yield of $Cs_2AgInCl_6$ double perovskite nanocrystals, *Nanoscale*, 2022, **14**, 15691–15700.

10 Y. Liu, X. Rong, M. Li, M. S. Molokeev, J. Zhao and Z. Xia, Incorporating rare-earth terbium(III) Ions into $Cs_2AgInCl_6$:Bi nanocrystals toward tunable photoluminescence, *Angew. Chem., Int. Ed.*, 2020, **59**, 11634–11640.

11 Y. Mahor, W. J. Mir and A. Nag, Synthesis and near-infrared emission of Yb-Doped $Cs_2AgInCl_6$ double perovskite microcrystals and nanocrystals, *J. Phys. Chem. C*, 2019, **123**, 15787–15793.

12 W. Lee, S. Hong and S. Kim, Colloidal synthesis of lead-Free silver–indium double-perovskite $Cs_2AgInCl_6$ nanocrystals and their doping with lanthanide Ions, *J. Phys. Chem.*, 2019, **123**, 2665–2672.

13 H. Arfin, J. Kaur, T. Sheikh, S. Chakraborty and A. Nag, $Bi^{3+}$-$Er^{3+}$ and $Bi^{3+}$-$Yb^{3+}$ co-doped $Cs_2AgInCl_6$ double perovskite near-infrared emitters, *Angew. Chem., Int. Ed.*, 2020, **59**, 11307–11311.

14 J. Liu, H. Rijckaert, M. Zeng, K. Haustraete, B. Laforce, L. Vincze, I. Van Driessche, A. M. Kaczmarek and R. Van Deun, Simultaneously excited downshifting/upconversion luminescence from lanthanide-doped core/shell fluoride nanoparticles for multimode anticounterfeiting, *Adv. Funct. Mater.*, 2018, **28**, 1707365.

15 D. Gao, D. Zhao, Y. Pan, R. Chai, Q. Pang, X. Zhang and W. Chen, Extending the color response range of $Yb^{3+}$ concentration-dependent multimodal luminescence in Yb/Er doped fluoride microrods by annealing treatment, *Ceram. Int.*, 2021, **47**, 32000–32007.

16 D. Gao, J. Gao, F. Gao, Q. Kuang, Y. Pan, Y. Chen and Z. Pan, Quintuple-mode dynamic anti-counterfeiting using multimode persistent phosphors, *J. Mater. Chem. C*, 2021, **9**, 16634–16644.

17 S. Wang, J. Qi, S. V. Kershaw and A. L. Rogach, Co-doping of cerium and bismuth into lead-free double perovskite $Cs_2AgInCl_6$ nanocrystals results in improved photoluminescence efficiency, *ACS Nanosci. Au*, 2022, **2**, 93–101.

18 H. Arfin, A. S. Kshirsagar, J. Kaur, B. Mondal, Z. Xia, S. Chakraborty and A. Nag, $ns^2$ electron ($Bi^{3+}$ and $Sb^{3+}$) doping in lead-free metal halide perovskite derivatives, *Chem. Mater.*, 2020, **32**, 10255–10267.

19 F. Locardi, M. Cirignano, D. Baranov, Z. Dang, M. Prato, F. Drago, M. Ferretti, V. Pinchetti, M. Fanciulli, S. Brovelli, L. De Trizio and L. Manna, Colloidal synthesis of double perovskite Cs2AgInCl6 and Mn-doped Cs2AgInCl6 nanocrystals, *J. Am. Chem. Soc.*, 2018, **140**, 12989–12995.

20 D. Manna, T. K. Das and A. Yella, Tunable and stable white light emission in $Bi^{3+}$-alloyed $Cs_2AgInCl_6$ double perovskite nanocrystals, *Chem. Mater.*, 2019, **31**, 10063–10070.

21 Y. Liu, Y. Jing, J. Zhao, Q. Liu and Z. Xia, Design optimization of lead-free perovskite $Cs_2AgInCl_6$:Bi nanocrystals with 11.4% photoluminescence quantum yield, *Chem. Mater.*, 2019, **31**, 3333–3339.

22 Y. Liu, M. S. Molokeev and Z. Xia, Lattice doping of lanthanide ions in $Cs_2AgInCl_6$ nanocrystals enabling tunable photoluminescence, *Energy Mater. Adv.*, 2021, 2585274.

23 C. Homann, L. Krukewitt, F. Frenzel, B. Grauel, C. Würth, U. Resch-Genger and M. Haase, NaYF4:Yb, Er/NaYF4 core/shell nanocrystals with high upconversion luminescence quantum yield, *Angew. Chem., Int. Ed.*, 2018, **57**, 8765–8769.

24 H. X. Mai, Y. W. Zhang, L. D. Sun and C. H. Yan, Highly efficient multicolor up-conversion emissions and their mechanisms of monodisperse NaYF4:Yb, Er core and core/shell-structured nanocrystals, *J. Phys. Chem. C*, 2007, **111**, 13721–13729.

25 Z. Rao, Q. Li, Z. Li, L. Zhou, X. Zhao and X. Gong, Ultra-high-sensitive temperature sensing based on $Er^{3+}$ and $Yb^{3+}$ co-doped lead-free double perovskite microcrystals, *J. Phys. Chem. Lett.*, 2022, **13**, 3623–3630.

26 Y. Pei, D. Tu, C. Li, S. Han, Z. Xie, F. Wen, L. Wang and X. Chen, Boosting near-infrared luminescence of lanthanide in $Cs_2AgBiCl_6$ double perovskites via breakdown of the local site symmetry, *Angew. Chem., Int. Ed.*, 2022, **61**, e202205276.

27 Z. Xu, L. Chen, L. Zhang, S. Jing, B. Zhuang, W. Xu and D. Chen, Yb/Er: $Cs_2Ag(In/Bi)Cl_6$ lead-free double perovskite for dual-modal optical temperature sensing, *J. Lumin.*, 2022, **248**, 118996.

28 K. Du, M. Zhang, Y. Li, H. Li, K. Liu, C. Li, J. Feng and H. Zhang, Embellishment of upconversion nanoparticles with ultrasmall perovskite quantum dots for full-color tunable, dual-modal luminescence anticounterfeiting, *Adv. Opt. Mater.*, 2021, **9**, 2100814.

29 P. J. Sugumaran, J. Zhang and Y. Zhang, Synthesis of stable core-shell perovskite based nano-heterostructures, *J. Colloid Interface Sci.*, 2022, **628**, 121–130.

30 H. Xiao, B. Liu, L. Qiu, G. Li, G. Zhang, D. Huang, Y. Zhao, C. Yang, F. Jiang, P. Dang, H. Lian, Z. Cheng and J. Lin, Core–shell structured upconversion/lead-free perovskite nanoparticles for anticounterfeiting applications, *Angew. Chem., Int. Ed.*, 2022, **61**, e202115136.

31 C. Zhang, J. Chen, L. Kong, L. Wang, S. Wang, W. Chen, R. Mao, L. Turyanska, G. Jia and X. Yang, Core/shell metal halide perovskite nanocrystals for optoelectronic applications, *Adv. Funct. Mater.*, 2021, **31**, 2100438.

32 N. Chen, T. Cai, W. Li, K. Hills-Kimball, H. Yang, M. Que, Y. Nagaoka, Z. Liu, D. Yang, A. Dong, C. Y. Xu, R. Zia and O. Chen, Yb- and Mn-doped lead-free double perovskite $Cs_2AgBiX_6$ (X = $Cl^-$, $Br^-$) nanocrystals, *ACS Appl. Mater. Interfaces*, 2019, **11**, 16855–16863.

33 E. Cui, X. Yuan, L. Tang, L. Yang, X. Yang, X. Liao, J. Tang, Y. Zhao, W. Sun, K. Liu, Y. Liu and J. Liu, Eu3+, Tb3+ doping induced tunable luminescence of Cs2AgInCl6 double perovskite nanocrystals and its mechanism, *Appl. Surf. Sci.*, 2023, **609**, 155472.

34 P. Capdevielle, A. Lavigne, D. Sparfel, J. Baranne-Lafont, K. C. Nguyen and M. Maumy, Mechanism of primary aliphatic

amines oxidation to nitriles by the cuprous chloride - dioxygen - pyridine system, *Tetrahedron Lett.*, 1990, **31**, 3305–3308.

35 Y. Xie, Y. Song, G. Sun, P. Hu, A. Bednarkiewicz and L. Sun, Lanthanide-doped heterostructured nanocomposites toward advanced optical anti-counterfeiting and information storage, *Light: Sci. Appl.*, 2022, **11**, 150.

36 J. Xu, W. Huang, P. Li, D. R. Onken, C. Dun, Y. Guo, K. B. Ucer, C. Lu, H. Wang, S. M. Geyer, R. T. Williams and D. L. Carroll, Imbedded nanocrystals of $CsPbBr_3$ in $Cs4PbBr_6$: Kinetics, enhanced oscillator strength, and application in light-emitting diodes, *Adv. Mater.*, 2017, **29**, 1703703.



 